Plasmonic Materials for Surface-Enhanced Sensing and Spectroscopy

Amanda J. Haes, Christy L. Haynes, Adam D. McFarland, George C. Schatz, Richard P. Van Duyne, and Shengli Zou

Abstract

Localized surface plasmon resonance (LSPR) excitation in silver and gold nanoparticles produces strong extinction and scattering spectra that in recent years have been used for important sensing and spectroscopy applications. This article describes the fabrication, characterization, and computational electrodynamics of plasmonic materials that take advantage of this concept. Two applications of these plasmonic materials are presented: (1) the development of an ultrasensitive nanoscale optical biosensor based on LSPR wavelength-shift spectroscopy and (2) the use of plasmon-sampled and wavelength-scanned surface-enhanced Raman excitation spectroscopy (SERES) to provide new insight into the electromagnetic-field enhancement mechanism.

Keywords: *localized surface plasmon resonance spectroscopy, nanosensing, plasmonic materials, surface-enhanced Raman spectroscopy.*

Introduction

Plasmonics is an emerging branch of nanophotonics that examines the properties of the collective electronic excitations in noble metal films or nanoparticles known colloquially as surface plasmons. The excitement of plasmonics lies in its potential to achieve highly miniaturized and sensitive photonic devices by controlling, manipulating, and amplifying light on the nanometer length scale.[1–3]

To date, a variety of passive plasmonic devices have been demonstrated, including filters,[1] waveguides,[1,3] polarizers,[4] Bragg reflectors,[1] and nanoscopic light sources.[5] On the horizon are active plasmonic devices, such as light-output enhancers for organic light-emitting diodes[6,7] as well as switches and modulators.[8] Furthermore, our rapidly improving understanding of the interactions between adsorbed molecules and plasmonic nanostructures (i.e., molecular plasmonics)[9] is having a significant impact on a broad spectrum of other applications, including nanoscale optical spectroscopy,[10] surface-enhanced Raman spectroscopy,[11] surface plasmon resonance sensing,[12,13] and nanolithography.[14]

There are two types of surface plasmon resonance—localized and propagating. This article will mostly be concerned with the former, which we term localized surface plasmon resonance (LSPR). This occurs in silver and gold nanoparticles in the 10–200 nm size range and results in amplification of the electric field **E** near the particle surfaces such that $|\mathbf{E}|^2$ can be 100–10,000 times greater in intensity than the incident field. The field has a spatial range on the order of 10–50 nm and is strongly dependent on nanoparticle size, shape, and local dielectric environment. Propagating plasmons, which are often called surface plasmon polaritons (SPPs), are associated with smooth, thin films of silver and gold with thicknesses in the 10–200 nm range. Propagating plasmons lead to smaller field enhancements (10–100 times) and a larger spatial range (~1000 nm).

This article will focus on the fabrication and characterization of plasmonic materials that show promise in chemical/biological sensing and surface-enhanced spectroscopy applications. In the first part, the simple, massively parallel method of nanosphere lithography (NSL) and its use in the fabrication of size- and shape-controlled nanostructures is briefly reviewed. Also, the essential physics of LSPR and the theoretical methods used to understand it are described, and key results concerning the short- and long-range distance dependences of the electromagnetic fields surrounding the nanoparticles are summarized. In the second part of this article, we focus on the relationship between LSPR spectroscopy and surface-enhanced Raman spectroscopy (SERS), as revealed by surface-enhanced Raman excitation spectroscopy (SERES). SERES provides a systematic, reproducible way to optimize the signal intensity in SERS experiments.

Nanosphere Lithography

Nanosphere lithography (NSL)[15] is a surprisingly powerful yet simple approach to the fabrication of nanoparticle arrays with precisely controlled shape, size, and interparticle spacing.

Nanosphere lithography (Figure 1) begins with the self-assembly of monodisperse polystyrene or SiO_2 nanospheres of diameter D to form a single- or double-layer colloidal crystal mask for material deposition. A substrate (Figure 1a) is prepared so that the nanospheres can freely move until they reach their lowest energy configuration. This is achieved by chemically modifying the nanosphere surface with a negative charge that is electrostatically repelled by a negatively charged substrate such as mica or chemically treated glass. As the solvent (water) evaporates, capillary forces draw the nanospheres together, and they crystallize into an hcp pattern on the substrate. As in all naturally occurring crystals, nanosphere masks include a variety of defects that arise as a result of nanosphere polydispersity, site randomness, point defects (vacancies), line defects (slip dislocations), and polycrystalline domains. Typical defect-free domain sizes are in the 10–100 μm range. Following self-assembly of the nanosphere mask, a metal or other material is then deposited by physical vapor deposition from a collimated source normal to the substrate through the nanosphere mask to a controlled thickness. The resulting surface is referred to as a metal (e.g., Ag) "film over nanosphere" (FON) surface. Ag FON surfaces are robust plasmonic materials for

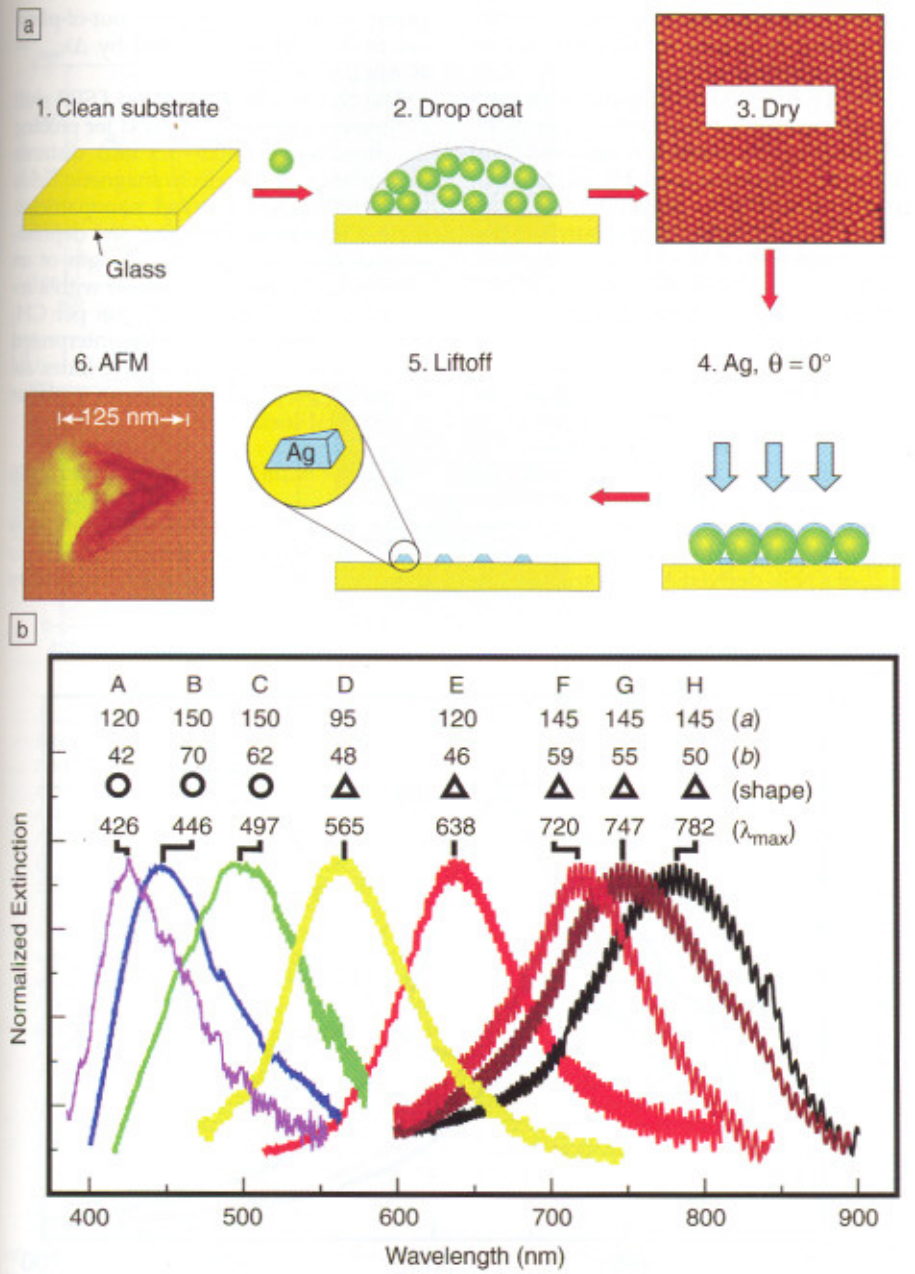

Figure 1. (a) Schematic representation of the nanosphere lithography (NSL) fabrication process. The AFM image in step 3 is 5 μm × 5 μm. (b) Size- and shape-tunable localized surface plasmon resonance spectra of various Ag nanoparticles (labeled A–H) fabricated by NSL. The wavelength of maximum extinction, λ_{max}, is changed by varying the in-plane width a *and out-of-plane height* b *of the nanoparticles.*

SERS applications.[16,17] If the nanosphere mask is removed, typically by sonicating the entire sample in a solvent, surface-confined nanoparticles are left behind that have a triangular footprint. In a typical NSL process, the deposition of 50 nm of Ag over a single-layer mask self-assembled from nanospheres with $D = 400$ nm produces nanotriangles with an in-plane width $a \approx 100$ nm, height $b \approx 50$ nm, and interparticle separation distance $d_{ip} \approx 230$ nm.

Size- and Shape-Tunable Localized Surface Plasmon Resonance Spectra

NSL-derived nanoparticles exhibit intense UV–visible extinction (i.e., the sum of absorption and scattering) bands that are not present in the spectrum of the bulk metal. Figure 1b shows that the LSPR spectra can easily be tuned all the way from the near-UV through the visible spectrum[18] and even into the mid-IR[19] by changing the size or shape (triangle or hemisphere) of the nanoparticles. Note that the LSPR bandwidth does not change significantly as the wavelength at peak maximum, λ_{max}, is tuned. Additionally, several other surprising LSPR optical properties have been discovered for NSL-derived Ag nanoparticles: (1) λ_{max} shifts by 2–6 nm per 1 nm variation in nanoparticle width or height,[18] (2) the molar decadic (tenfold) extinction coefficient is $\varepsilon = 3 \times 10^{11}$ M^{-1} cm^{-1},[18] (3) the LSPR oscillator strength per atom is equivalent to that of atomic silver in gas or liquid phases,[18] (4) resonant Rayleigh scattering[20,21] occurs with an efficiency equivalent to that of 10^6 fluorophors,[22] and (5) local electromagnetic fields are amplified by factors of $|\mathbf{E}|^2 \approx 10^4$, leading to intense signals in all surface-enhanced spectroscopies.[11]

Fundamentals of Localized Surface Plasmon Resonance Spectroscopy

The simplest theoretical approach available for modeling the optical properties of nanoparticles is classical electrodynamics (i.e., solving Maxwell's equations with the metal dielectric constant taken from bulk measurements). For spherical particles, this leads to the following (Mie theory) expression for the extinction coefficient $E(\lambda)$ in the long-wavelength limit:[23]

$$E(\lambda) = \frac{24\pi N_A a^3 \varepsilon_m^{3/2}}{\lambda \ln(10)} \times \left[\frac{\varepsilon_i}{(\varepsilon_r + 2\varepsilon_m)^2 + \varepsilon_i^2} \right]. \quad (1)$$

Here, N_A is the areal density of the nanoparticles, a is the radius of the metallic nanosphere, ε_m is the dielectric constant of the medium surrounding the nanosphere (assumed to be a positive, real number), λ is the wavelength, and ε_r and ε_i are the real and imaginary parts of the metal dielectric function. This formula predicts a resonant peak when $\varepsilon_r = -2\varepsilon_m$, which for silver and gold occurs in the visible portion of the spectrum. In addition, any change in the dielectric constant of the medium (e.g., when molecules adsorb on the particle) leads to a change in the resonance wavelength.

When one considers spheroidally shaped particles, the term $\varepsilon_r + 2\varepsilon_m$ in the denominator in Equation 1 is replaced by $\varepsilon_r + \chi\varepsilon_m$, where χ is a parameter that depends on the shape of the spheroid, increasing from 2 for a sphere to 17 for a spheroid with an aspect ratio of 5:1. This leads to strong de-

pendence of λ_{max} on particle shape, and there is also a strong size dependence that arises from electrodynamic effects that are not contained in Equation 1. In addition, many of the samples considered in this work contain an ensemble of nanoparticles that are supported on a substrate, leading to a dependence on interparticle spacing[2] and substrate dielectric constant.[24]

Electrodynamic Calculations

Equation 1 provides useful insight, but it only applies to spherical particles. In order to describe particles like those pictured in Figure 1a, it is necessary to use a numerical method. Several methods have been developed for solving Maxwell's equations using finite-element-based approaches, and one that we have found to be particularly useful is the discrete dipole approximation (DDA).[25–27] In this method, the particle is subdivided into an array of cubical, polarizable elements. When a plane wave field is applied to the particle, the resulting induced polarizations in the elements are calculated, and from these the extinction and local fields are determined. Figure 2a shows extinction cross sections that have been calculated with this approach for several particle shapes, all for silver particles with the same volume. This shows that a sphere has a plasmon nearer the blue end of the spectrum (Figure 2b), and the particles with points (cubes, prisms, pyramids) are nearer the red end of the spectrum (Figures 2c and 2d).

The electromagnetic (EM) mechanism of SERS[11] predicts an enhancement factor proportional to $|E(\omega)|^2|E(\omega')|^2$, where ω and ω' are the incident and Stokes-shifted frequencies, respectively. To estimate the enhancement factor, in Figures 2b–2d we show contours of $|E|^2$ around three of the particles for wavelengths corresponding to λ_{max} and for polarizations that lead to the largest $|E|^2$. These figures show that the peak field for a sphere is on the order of 10^2, while that for the tetrahedron is 10^4. If we approximate the enhancement factor as $|E(\omega)|^4$, we see that the highest enhancements are on the order of 10^8, which, as noted later, is about what is found for NSL-derived particles.

Distance Dependence of the Localized Surface Plasmon Resonance

The electrodynamics results in Figure 2 show that the electromagnetic fields surrounding Ag nanoparticles excited at λ_{max} drop off quickly as one moves a few nanometers away from the particle surface. How can the range of these fields be measured experimentally? Scanning near-field optical microscopy is certainly a possibility; however, the resolution currently obtainable (~10 nm) would only provide a rough picture.

We have pursued an alternative strategy to experimentally measure the range of the electromagnetic fields. It is apparent from Equation 1 that λ_{max} of noble metal nanoparticles is highly dependent on the dielectric properties of the surrounding environment. For NSL-derived Ag nanoparticles, it has been demonstrated experimentally that λ_{max} is a linear function of the solvent refractive index, n_m (where the external dielectric constant, ε_m, is equal to n_m^2) with a slope of approximately 200 nm per refractive index unit (RIU, defined as a change of 1 in the refractive index).[28] In addition, λ_{max} is responsive to molecule-induced changes in the local dielectric environment. For example, the chemisorption of one monolayer of hexadecanethiol causes λ_{max} of a NSL-derived Ag nanotriangle (in-plane width a = 100 nm, out-of-plane height b = 50 nm) to shift by $\Delta\lambda_{max}$ = 40 nm (Figure 3a).[29,30]

The chemisorption-induced LSPR shift experiment provides a method for probing the short-range (~0.5–3.5 nm) distance dependence of the electromagnetic fields surrounding NSL-derived nanoparticles. Figure 3c demonstrates that the dependence of $\Delta\lambda_{max}$ on the chain length of an alkanethiol monolayer is linear with a remarkably large slope of 3.1 nm per CH_2 unit.[29,30] These results can be interpreted using a model of the refractive-index response of propagating SPPs on a planar noble metal surface:[31]

$$\Delta\lambda_{max} = m\Delta n[1 - \exp(-2d/l_d)], \quad (2)$$

where $\Delta\lambda_{max}$ is the wavelength shift, m is the refractive-index sensitivity, Δn is the change in refractive index induced by

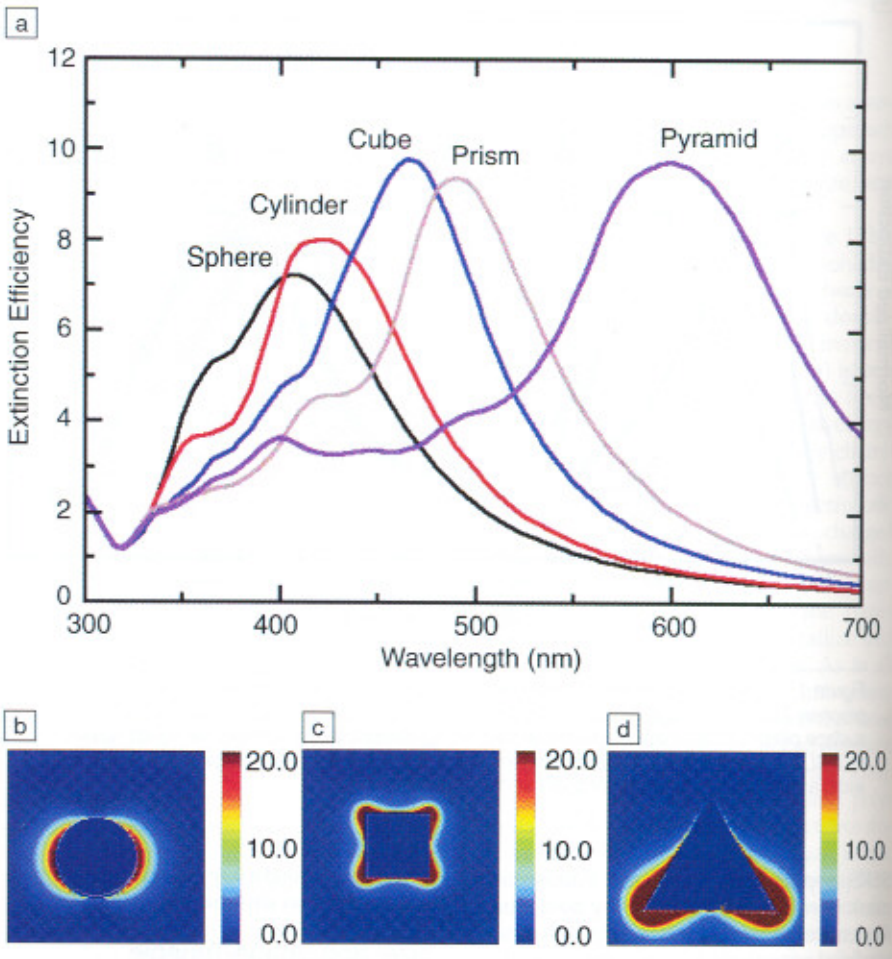

*Figure 2. (a) Extinction efficiency (ratio of cross section to effective area) of silver nanoparticles in vacuum having the shapes indicated. Each particle has the same volume, taken to be that of a sphere with a radius of 50 nm. $|E|^2$ contours (**E** is electric field) for a (b) sphere, (c) cube, and (d) pyramid, plotted for wavelengths corresponding to the plasmon peak in (a), with peak $|E|^2$ values of 54, 745, and 9770, respectively.*

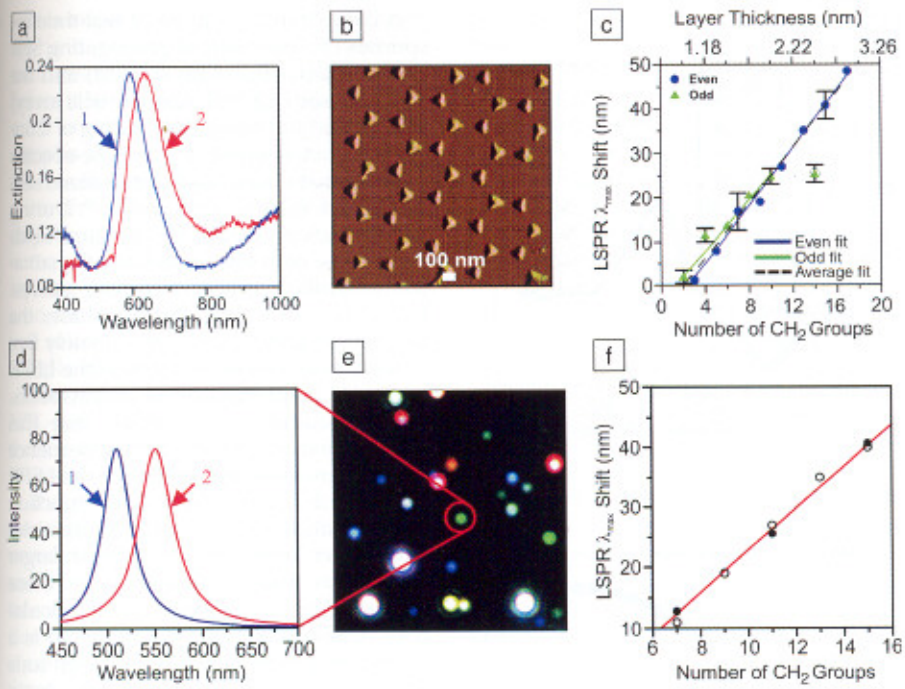

Figure 3. (top row) Localized surface plasmon resonance (LSPR) spectroscopy of a Ag nanoparticle array fabricated by nanosphere lithography in a N_2 environment: (a) Extinction spectrum of the array (curve 1) before chemical modification, wavelength of extinction maximum λ_{max} = 594.8 nm, and (curve 2) after modification with 1 mM hexadecanethiol, λ_{max} = 634.8 nm. (b) Tapping-mode atomic force microscopy (AFM) image of the array in (a); nanosphere diameter D = 390 nm, deposited mass thickness d_m = 50 nm; Ag on mica substrate; scan area, 3.0 μm^2. After solvent annealing, nanoparticle in-plane width is 100 nm and out-of-plane height is 51 nm. (c) Alkanethiol chain length dependence on the LSPR spectral peak shifts for the array. Even and odd carbon chain lengths are depicted with different symbols to emphasize the difference in the terminal bond orientation with respect to the substrate, which leads to different observed trends for the two cases. (bottom row) LSPR spectroscopy of single Ag nanoparticles produced by chemical synthesis: (d) scattering spectrum of a single Ag nanoparticle (curve 1) before chemical modification, λ_{max} = 510.2 nm, and (curve 2) after modification with 1 mM hexadecanethiol, λ_{max} = 550.9 nm. The circled nanoparticle in (e) produced the signal for these curves. (e) Dark-field resonant Rayleigh scattering image of a random array of chemically synthesized Ag nanoparticles (image dimensions, 130 $\mu m \times 130 \mu m$). (f) Alkanethiol chain length dependence on the LSPR spectral peak shifts for a single Ag nanoparticle. The open circles represent an overlay of the array data from (c). The solid circles are single nanoparticle measurements.

an adsorbate, d is the effective adsorbate layer thickness, and l_d is the characteristic electromagnetic-field decay length. This model assumes exponential decay of the electromagnetic field normal to the planar surface, which is accurate for a SPP, but is undoubtedly an oversimplification for the electromagnetic fields associated with noble metal nanoparticles. Nevertheless, Equation 2 does a remarkably good job of accounting for the data in Figure 3c if one assumes a value l_d = 5–6 nm. We will return to a justification of this value in a moment.

Recently, it has become possible to use dark-field resonant Rayleigh scattering to perform the $\Delta\lambda_{max}$ measurement for isolated *single* nanoparticles, and it was found that for chemically synthesized Ag triangular prisms (Figure 3e), $\Delta\lambda_{max}$ is a linear function of the refractive index of the external medium (Figure 3d) with a slope of ~200 nm/RIU.[32] In addition, the same LSPR shift of ~40 nm as seen for the NSL particle array was observed for a monolayer of hexadecanethiol on a single particle; more important, the dependence of $\Delta\lambda_{max}$ on the chain length of the alkanethiol monolayer (Figure 3f) was found to be linear, with a large slope of 3.5 nm per CH_2 unit.[32]

The similarity of the adsorbate-induced LSPR shift behavior for both NSL-derived nanoparticle arrays and single nanoparticles leads to the following important conclusions: (1) the short-range distance dependences for both systems can be described by Equation 2, and (2) interparticle coupling effects are minimal at the d_{ip} values imposed by the NSL nanofabrication technique. In addition, it should be pointed out that from the viewpoint of chemical sensing, these single-nanoparticle LSPR shift results are truly remarkable. Based on the average surface area of the nanoparticles prepared and the monolayer packing density of molecules on Ag, this saturation response corresponds to the detection of fewer than 60,000 surface-confined molecules of hexadecanethiol. Additional experiments (not described here) demonstrate a limit of detection of ~2000 molecules.[32] The real-time kinetics of adsorbates binding to single nanoparticles is also accessible from this experiment.[32]

LSPR spectroscopy can also be used to probe the long-range (up to 40 nm) distance dependence of the electromagnetic fields surrounding NSL-derived Ag nanoparticles.[33] Figure 4 (see 4a and the solid triangles in 4c) shows that the dependence of $\Delta\lambda_{max}$ on the thickness of multilayer adsorbate shells synthesized through the interaction of $HOOC(CH_2)_{10}SH$ and Cu^{2+} is nonlinear. The multilayer thickness required to saturate the LSPR shift response was found to be dependent on the composition (Ag versus Au), shape (triangle versus hemisphere), in-plane width, and out-of-plane height of the nanoparticles. These results verify that the linear distance dependence found in the case of alkanethiol monolayers was the thin-shell limit of a longer-range, nonlinear dependence. They can be understood on the basis of an exponentially decaying electromagnetic field with l_d in the range of 5–6 nm for Ag nanotriangles ($a \approx 100$ nm, $b \approx 50$ nm). A more accurate simulation of the data has been provided by DDA calculations,[33] and the results are in quantitative agreement with experiment. Comparison of the long-range LSPR spectroscopy results for Ag (Figure 4a and solid circles in 4d) versus Au (Figure 4b and red triangles in 4d) shows that Ag has a longer spatial electromagnetic range and is more sensitive to adsorbates than Au.

Nanoscale Optical Biosensors Based on LSPR Spectroscopy

The LSPR wavelength shift response, $\Delta\lambda_{max}$, has been used to develop a new class of nanoscale optical biosensors.[34–38] Two model systems, biotin–streptavidin[34] and biotin–anti-biotin,[35] were studied to illustrate the desirable attributes of LSPR-based nanoscale affinity biosensors. Streptavidin, a tetrameric protein, can bind up to four biotinylated molecules (i.e., antibodies, inhibitors, nucleic acids, etc.) with minimal impact on its biological activity, and therefore it provides a ready pathway for extending the analyte accessibility of the LSPR nanobiosensor. Anti-biotin, an antibody,

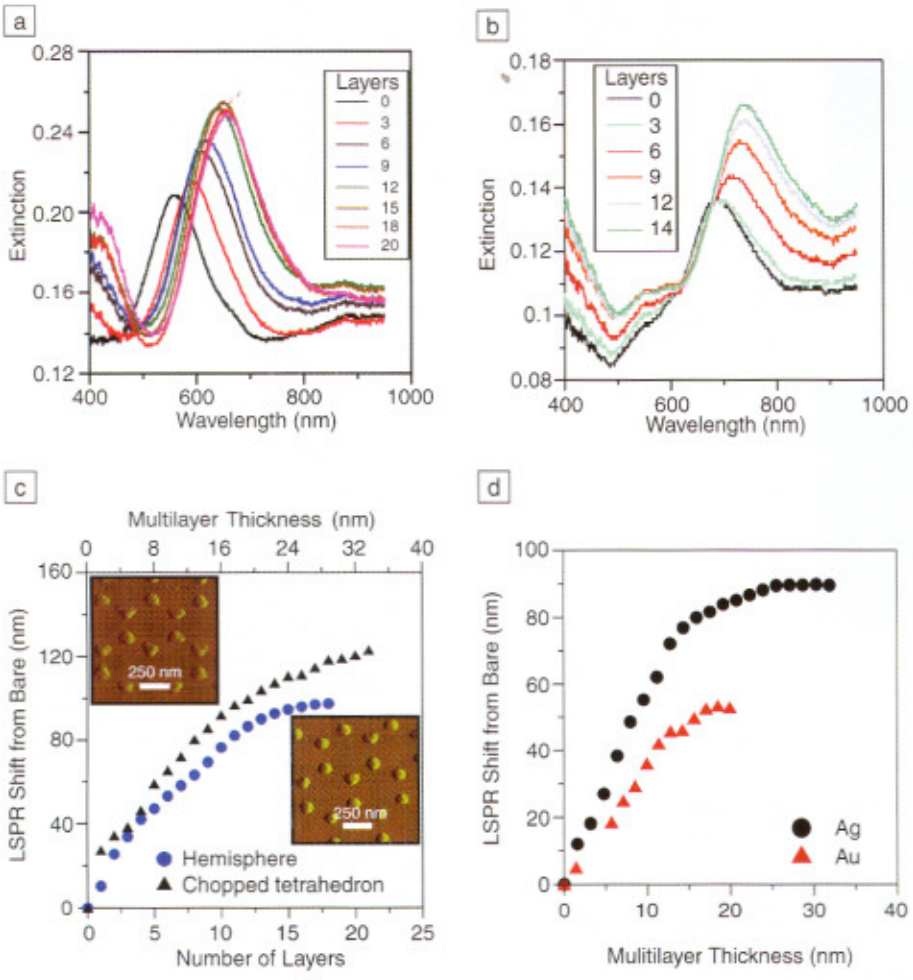

Figure 4. Localized surface plasmon resonance (LSPR) spectra for Ag and Au nanoparticles fabricated by nanosphere lithography. Long-range distance dependence: (a) Ag nanoparticles (in-plane width a = *100 nm, out-of-plane height* b = *50.0 nm) for 0–20 layers of* Cu^{2+}/HS–$(CH_2)_{10}$COOH; *(b) Au nanoparticles (*a = *70 nm,* b = *50.0 nm) for 0–14 layers of* Cu^{2+}/HS–$(CH_2)_{10}$COOH. *(c) Shape dependence for Ag nanoparticles: (solid triangles) LSPR shift versus number of layers in the self-assembled monolayer (SAM) thickness for solvent-annealed Ag nanoparticles; (blue circles) LSPR shift versus number of layers in the SAM thickness for thermally annealed (600°C for 1 h) Ag nanoparticles. (inset, upper left) Atomic force microscopy (AFM) image of solvent-annealed nanoparticles (*a = *114 nm,* b = *54 nm). (inset, lower right) AFM image of thermally annealed nanoparticles (*a = *110 nm,* b = *61 nm). (d) Composition dependence: (solid circles) LSPR shift versus layer thickness for Ag nanoparticles (*a = *70 nm,* b = *50.0 nm); (red triangles) LSPR shift versus layer thickness for Au nanoparticles (*a = *70 nm,* b = *50.0 nm).*

provides a straightforward platform to extend the LSPR nanosensor technology to immunoassay technology. The $\Delta\lambda_{max}$ for biotin-functionalized Ag NSL nanoparticle arrays was measured as a function of the concentration of streptavidin (SA) over the concentration range 10^{-15} M < [SA] < 10^{-6} M. Fitting the data to the theoretical normalized response expected for 1:1 binding of a ligand to a multivalent receptor with different sites but invariant affinities yielded the following values: saturation response R_{max} = 26.5 nm, surface-confined thermodynamic binding constant $K_{a,surf} = 10^{11}$ M^{-1}, and limit of detection LOD < 1 pM SA.[34] Similarly, the LSPR response curve for the binding of anti-biotin (AB) to biotin-functionalized Ag NSL nanoparticles was measured, and the data analysis yielded R_{max} = 38.0 nm, $K_{a,surf} = 4.5 \times 10^7$ M^{-1}, and LOD $< 7 \times 10^{-10}$ M AB.[35] As predicted, the LOD of the nanobiosensor studied is lower for systems with higher binding affinities, such as for the well-studied biotin–streptavidin couple, and higher for systems with lower binding affinities, as seen in the anti-biotin system.

A comparative analysis of real-time responses of a commercial propagating SPR sensor (planar thin film of gold) and the LSPR sensor (Ag NSL nanoparticle array) was carried out using the binding of Concanavalin A (ConA), a mannose-specific plant lectin, to mannose-functionalized self-assembled monolayers (SAMs).[36] During the association phase in the real-time binding studies, both sensors exhibited qualitatively similar signal-versus-time curves. However, in the dissociation phase, the SPR sensor showed an approximately five times greater loss of signal than the LSPR sensor. A comprehensive set of nonspecific binding studies demonstrated that this signal difference was not the consequence of greater nonspecific binding to the LSPR sensor, but rather a systematic function of nanoparticle structure. Ag nanoparticles with larger aspect ratios showed larger dissociation phase responses than those with smaller aspect ratios. DDA calculations demonstrated that this response is a consequence of the similarity in length scale between the electromagnetic-field decay length and the physical size of ConA.[36]

Recently, the LSPR sensor has been successfully used for the detection of an Alzheimer's disease biomarker from both synthetic[37,38] and human patient[38] samples (see also the article by Thaxton et al. in this issue). In this work, the interactions between the biomarker (antigen), amyloid-β derived diffusible ligands (ADDLs), and specific anti-ADDL antibodies were studied. Using the sandwich assay format, the LSPR sensor provided quantitative binding information for both antigen and second antibody detection that permits the determination of ADDL concentration. This unique capability offers the possibility of analyzing the aggregation mechanisms of this putative Alzheimer's disease pathogen at physiologically relevant monomer concentrations. Monitoring the LSPR-induced shifts from both ADDLs and a second polyclonal anti-ADDL antibody as a function of ADDL concentration reveals two ADDL epitopes (the exact binding site on an antigen that binds to an antibody) that have binding constants to the specific anti-ADDL antibodies of 7.3×10^{12} M^{-1} and 9.5×10^8 M^{-1}. Furthermore, this study demonstrated for the first time that the LSPR nanosensor was successful at analyzing human brain extract and cerebrospinal fluid (CSF) samples. Examination of these results from both Alzheimer's disease and control patients reveals that the LSPR nanosensor provides new information relevant to the understanding and possible diagnosis of Alzheimer's disease. This exciting advance is one of the first examples in which nanotechnology has been applied to clinical materials for biomolecular diagnostics.[38]

It is important to note that this technology is in its infancy. There are at least two main research objectives that must be met before it becomes available. First, the sensor must undergo rigorous testing using CSF samples from many more patients. In order for this objective to be met, we must integrate this technology with a redesigned chip. Currently, approximately 250 μl of CSF is required for each assay. Because spinal taps are painful, it is ideal to minimize the amount of sample needed. By incorporating microfluidics and miniaturizing the sample cell, this objective will be met.

The examples just given all involved NSL-derivatized Ag nanoparticle arrays as the sensor platform. It has now been demonstrated that all of the outstanding attributes of the propagating SPR sensor, the "gold standard" in optical biosensing, are retained or exceeded in a single-nanoparticle sensor.[32,39] Dark-field LSPR scattering spectroscopy and microscopy were used to demonstrate zeptomole (10^{-21}) sensitivity coupled with real-time kinetic analysis.[32] Streptavidin biosensing has also been demonstrated on single Ag nanoparticles. A 12.7 nm redshift in the LSPR λ_{max} arises from the detection of <700 streptavidin molecules.[40]

Surface-Enhanced Raman Spectroscopy

The local electromagnetic fields that accompany photon excitation of the LSPR are a key factor leading to the intense signals observed in all surface-enhanced spectroscopies.[11] Surface-enhanced Raman spectroscopy (SERS) is characterized by an ensemble-averaged intensity enhancement factor, EF, of ~10^6, for analytes bound to noble metal surfaces that possess random roughness,[41] or EF ≈ 10^7–10^8, for surfaces with intentionally nanofabricated feature sizes in the ~100 nm range.[42] Recent reports of single-molecule detection[43,44] using SERS on Ag nanoparticle clusters have rejuvenated interest in this widely used analytical technique. A clear understanding of the mechanism responsible for the enormous enhancement factors (~10^{14}–10^{15}) observed in single-molecule SERS remains elusive.

The electromagnetic (EM) mechanism of SERS mentioned earlier predicts that there is a well-defined relationship between the LSPR spectrum and the SERES spectrum of a SERS-active surface. In particular, very specific quantitative predictions for the magnitude of the enhancement factor on nanoparticle size, shape, and local dielectric environment are made. Wavelength-scanned SERES experiments on microfabricated surfaces were carried out in the early 1980s at Bell Laboratories,[45,46] with a view toward verifying these predictions of the EM mechanism. Both as a consequence of experimental difficulty and the dissolution of the Bell group, many EM predictions remain purely in the domain of theory. The plasmonic materials that are now readily available from NSL and electron-beam lithography (EBL) provide a new platform for the detailed study of the electromagnetic-field enhancement mechanism associated with SERS. Consequently, there is renewed experimental effort in SERES seeking to verify various aspects of the EM theory.

We will now discuss some recent results from our laboratory obtained using two approaches—plasmon-sampled (PS)[42] and wavelength-scanned (WS) SERES. WS-SERES requires both a broadly tunable laser and detection system. This is not commonly available; however, with the size- and shape-tunable LSPR spectra obtainable with NSL- or EBL-derived plasmonic materials, this problem can be circumvented. NSL and EBL are used to prepare many samples with different LSPR λ_{max} values. Each sample is thoroughly characterized structurally by atomic force microscopy or scanning electron microscopy. Correlated, spatially resolved LSPR and SER spectra are measured with a single excitation wavelength at multiple locations on each sample using a Raman microscope. Figure 5 shows representative LSPR spectra (Figures 5a–5c) and SERS spectra (Figures 5d–5f) for benzenethiol adsorbed on NSL-fabricated Ag nanoparticles excited at three common, fixed, excitation wavelengths. The SERS enhancement factors for Figures 5d–5f are 7.6 × 10^7, 6.3 × 10^7, and 9.0 × 10^7, respectively,[42] which are results that roughly agree with theoretical estimates (the electrodynamic calculations described earlier). PS-SERES plots (enhancement factor versus LSPR λ_{max}) for the 1575 cm^{-1} band of benzenethiol excited at three different laser wavelengths each showed a well-defined maximum

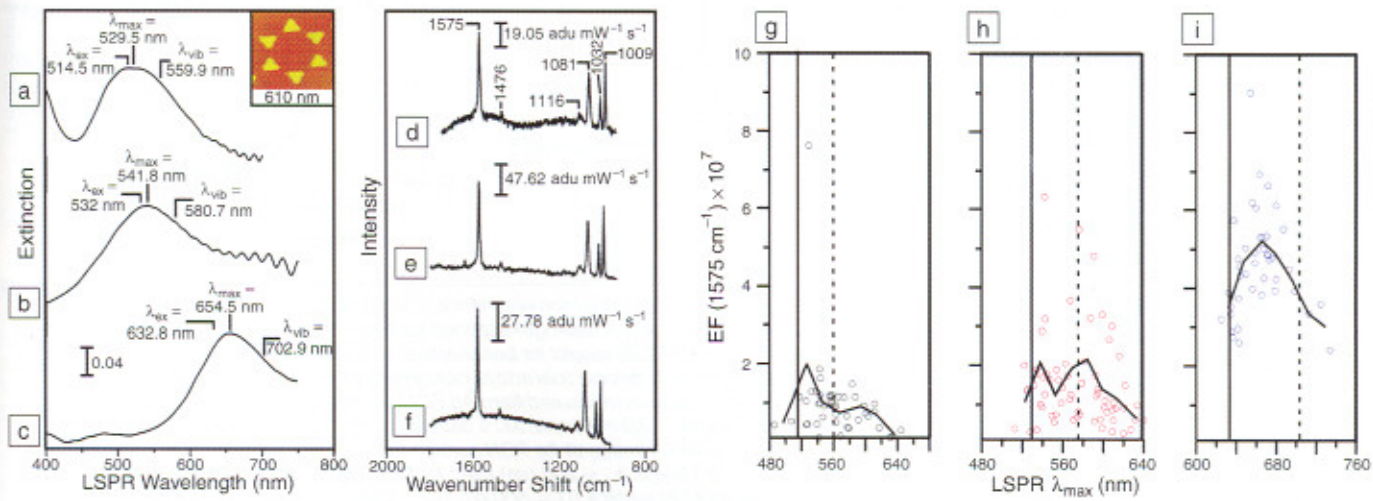

Figure 5. (a)–(f) Correlated, spatially resolved, localized surface plasmon resonance (LSPR) and surface-enhanced Raman spectroscopy (SERS) results for benzenethiol adsorbed on Ag nanoparticle arrays fabricated by nanosphere lithography. (a), (d) Ag nanoparticles fabricated with nanosphere diameter D = 280 nm and deposited mass thickness d_m = 36 nm, probed with an excitation wavelength λ_{ex} = 514.5 nm, power = 0.7 mW. A representative atomic force micrograph of the substrate is shown in the inset. (b), (e) Ag nanoparticles fabricated with D = 280 nm, d_m = 36 nm, probed with λ_{ex} = 532.0 nm, power = 0.7 mW. (c), (f) Ag nanoparticles fabricated with D = 400 nm, d_m = 56 nm, probed with λ_{ex} = 632.8 nm, power = 1.2 mW. (g)–(i) Plasmon-sampled surface-enhanced Raman excitation spectroscopy (PS-SERES) results for the 1575 cm^{-1} band of benzenethiol with three different excitation wavelengths: (g) λ_{ex} = 514.5 nm, (h) λ_{ex} = 532.0 nm, and (i) λ_{ex} = 632.8 nm. For each λ_{ex}, both the wavelength location of the excitation (solid line) and the scattering (dashed line) are marked. The overlaid curves represent the bin-averaged values of the LSPR λ_{max} and the enhancement factor. Bin widths are (g) 24 nm, (h) 16 nm, and (i) 16 nm.

representing the highest intensity SERS signal (Figures 5g–5i).[42] In each case, these PS SERES spectra follow the behavior predicted by the EM theory, that is, the largest enhancement factor occurs when the energy corresponding to the LSPR maximum is located near the midpoint between the energy of laser excitation and the energy of the Raman photons. These results unambiguously demonstrate (1) a systematic approach to the optimization of SERS spectra on nanoparticle substrates and (2) that large, ensemble-averaged, SERS enhancement factors ($\sim 1 \times 10^8$) are readily obtainable from Ag NSL-derived nanoparticle array surfaces. Recently, these results have been corroborated using Au nanoparticle array surfaces fabricated by EBL.[47]

Figure 6a shows the SERS spectrum of benzenethiol adsorbed on a Ag FON surface. The nanostructure of Ag FON surfaces can be quantitatively characterized by atomic force microscopy (Figures 6b and 6c). Ag FON surfaces have a nanostructure size distribution that is less broad than that of a randomly roughened surface but not as narrow as a NSL-derived surface. Consequently, Ag FON surfaces have well-defined LSPR spectra (Figures 6d and 6e, solid curves), albeit broader than the LSPR spectra for Ag NSL-derived nanoparticle arrays. WS SERES spectra for the 1081 cm^{-1} band of benzenethiol are shown in Figures 6d and 6e (data points). Using neat liquid benzenethiol as the normal Raman standard, the peak enhancement factor values were calculated to be 2.7×10^6 and 1.9×10^6 for Figure 6d and 6e, respectively. Two different behaviors are observed in the WS-SERES spectra for these surfaces. In one case, the WS-SERES spectrum peaks to the red of the LSPR spectrum (Figure 6d, data points) and in the other, it tracks the LSPR spectrum (Figure 6e, data points). This outcome is attributed to the different nanostructure size distributions for each surface. From a practical perspective, we point out that it is not yet possible to determine the optimum laser excitation wavelength for an Ag FON without doing SERES.

Figure 6f shows the SERS spectrum of benzenethiol adsorbed on a Ag NSL-derived nanoparticle array surface. A typical atomic force micrograph of a Ag NSL surface is shown in the inset in Figure 6g. The LSPR spectrum of a Ag NSL array is shown in Figure 6g (solid red line), along with the corresponding WS-SERES spectrum for the 1081 cm^{-1} band of benzenethiol adsorbed on the same Ag NSL array (data points). The peak enhancement factor for the 1081 cm^{-1} band of benzenethiol adsorbed on this surface is 1.9×10^7, again using neat liquid benzenethiol as the normal Raman standard. Note that the peak

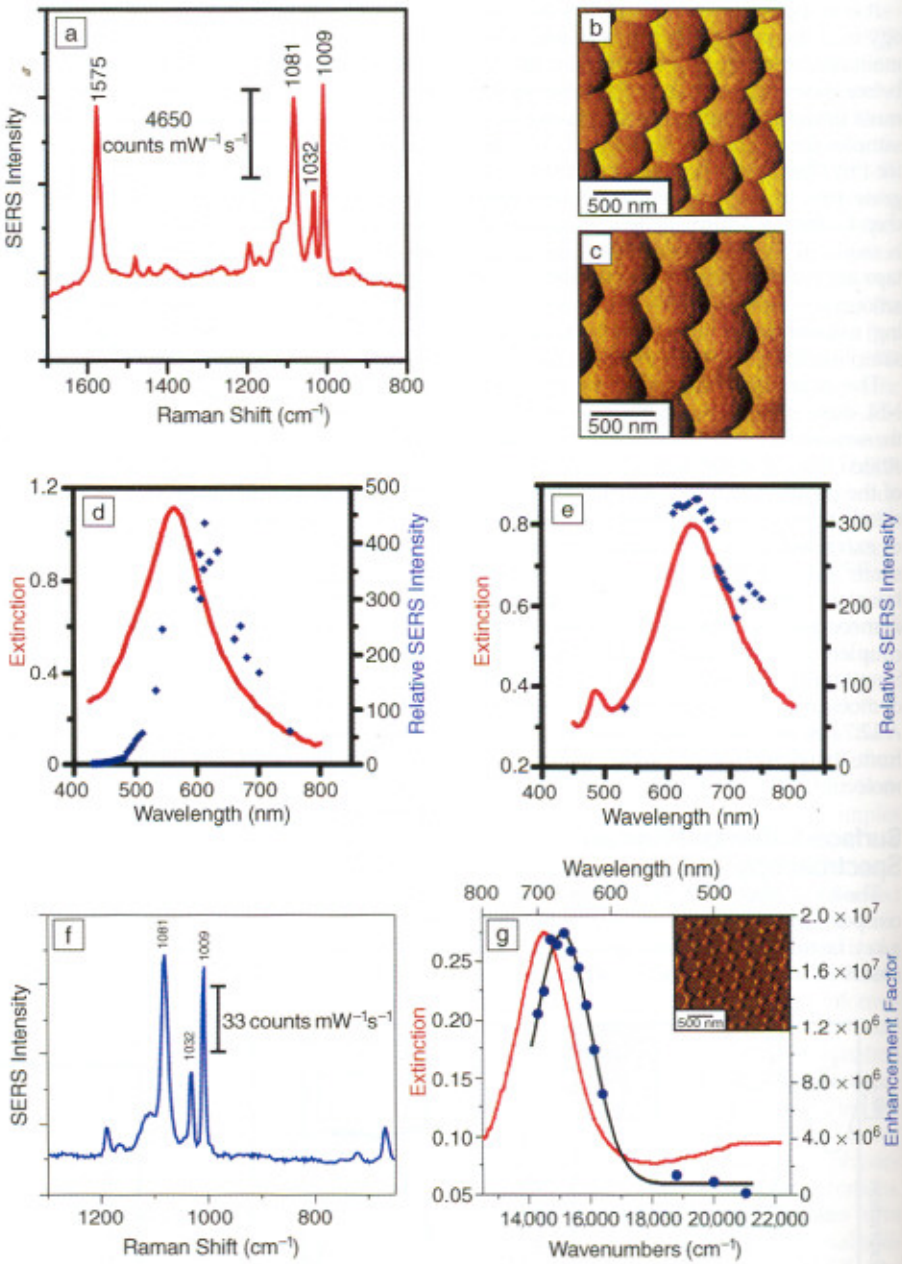

Figure 6. Localized surface plasmon resonance (LSPR), surface-enhanced Raman spectroscopy (SERS), and wavelength-scanned surface-enhanced Raman excitation spectroscopy (WS-SERES) results for benzenethiol adsorbed on Ag film-over-nanosphere (Ag FON) surfaces and nanoparticle arrays fabricated by nanosphere lithography (NSL). (a) SERS spectrum measured from Ag FON surface with excitation wavelength λ_{ex} = 532 nm, power = 3.0 mW, and 100 s data acquisition time. (b) Contact-mode atomic force microscopy (AFM) image of Ag FON surface (nanosphere diameter D = 410 nm, deposited mass thickness d_m = 200 nm) used for SERS in (a). (c) Contact-mode AFM image of Ag FON surface (D = 500 nm, d_m = 250 nm) used for WS-SERES in (e). (d) LSPR spectrum (solid line, λ_{max} = 562 nm, FWHM = 144 nm) and WS-SERES spectra (data points) for the 1081 cm^{-1} band of benzenethiol measured from the Ag FON surface in (b). (e) LSPR spectrum (solid line, λ_{max} = 638 nm, FWHM = 131 nm) and WS-SERES spectra (data points) for the 1081 cm^{-1} band of benzenethiol measured from Ag FON surface in (c). (f) SERS spectrum measured from Ag nanoparticle array surface (λ_{ex} = 532 nm, power = 3.0 mW, 100 s data acquisition time). (g) LSPR spectrum (solid line, λ_{max} = 688 nm, FWHM = 95 nm) and WS-SERES spectra (data points) for the 1081 cm^{-1} band of benzenethiol measured from a Ag nanoparticle array surface. (inset) Tapping-mode AFM image of a representative array surface.

of the WS-SERES spectrum is blueshifted by 613 cm^{-1} (76 meV) with respect to the LSPR λ_{max}. The blueshift is an important prediction of EM theory that has not been previously observed. The results in Figures 5 and 6 are, to the best of our knowledge, the first correlated LSPR and SERES measurements for a nanofabricated surface.[48,49]

Conclusions

The results presented here demonstrate the strength and versatility of silver and gold nanoparticles for biosensing based on extinction and surface-enhanced Raman spectroscopy and on single-particle Rayleigh scattering. These capabilities are based on the unique optical properties of localized surface plasmon resonances, including their sensitivity to particle shape and size, and to local changes in the surrounding refractive index due to molecular adsorption. In addition, plasmon excitation leads to strong local field enhancements that yield 10^8 enhancements in SERS. For all of these properties, theory can be used to provide important guidance to the design of these experiments. Recent theoretical work has suggested that new directions for nanoparticle-based sensing may be developed for interacting nanoparticle structures, including nanoparticle dimers[50] and large-scale arrays.[51] Thus, there is much yet to do in this field.

Acknowledgments

The authors gratefully acknowledge support from the Air Force Office of Scientific Research MURI program (grant F49620-02-1-0381), the National Science Foundation (EEC-0118025, DMR-0076097, CHE-0414554), the Institute for Bioengineering and Nanoscience in Advanced Medicine at Northwestern University, and the National Institutes of Health (1 R21 DK066990-01A1).

References

1. W.L. Barnes, A. Dereux, and T.W. Ebbesen, *Nature* **424** (2003) p. 824.
2. C.L. Haynes, A.D. McFarland, L. Zhao, R.P. Van Duyne, G.C. Schatz, L. Gunnarsson, J. Prikulis, B. Kasemo, and M. Käll, *J. Phys. Chem. B* **107** (2003) p. 7337.
3. S.A. Maier, P.G. Kik, H.A. Atwater, S. Meltzer, E. Harel, B.E. Koel, and A.A.G. Requicha, *Nature Mater.* **2** (2003) p. 229.
4. C.L. Haynes and R.P. Van Duyne, *Nano Lett.* **3** (2003) p. 939.
5. H.J. Lezec, A. Degiron, E. Devaux, R.A. Linke, L. Martin-Moreno, F.J. Garcia-Vidal, T.W. Ebbesen, *Science* **297** (2002) p. 820.
6. L.H. Smith, J.A.E. Wasey, and W.L. Barnes, *Appl. Phys. Lett.* **84** (2004) p. 2986.
7. S. Wedge, J.A.E. Wasey, W.L. Barnes, and I. Sage, *Appl. Phys. Lett.* **85** (2004) p. 182.
8. P. Andrew and W.L. Barnes, *Science* **306** (2004) p. 1002.
9. R.P. Van Duyne, *Science* **306** (2004) p. 985.
10. B. Pettinger, B. Ren, G. Picardi, R. Schuster, and G. Ertl, *Phys. Rev. Lett.* **92** 096101 (2004).
11. G.C. Schatz and R.P. Van Duyne, in *Handbook of Vibrational Spectroscopy, Vol. 1* (Wiley, New York, 2002) p. 759.
12. A.J. Haes and R.P. Van Duyne, *Anal. Bioanal. Chem.* **379** (2004) p. 920.
13. J.M. Brockman, B.P. Nelson, and R.M. Corn, *Ann. Rev. Phys. Chem.* **51** (2000) p. 41.
14. W. Srituravanich, N. Fang, C. Sun, Q. Luo, and X. Zhang, *Nano Lett.* **4** (2004) p. 1085.
15. J.C. Hulteen and R.P. Van Duyne, *J. Vac. Sci. Technol., A* **13** (1995) p. 1553.
16. L.A. Dick, A.D. McFarland, C.L. Haynes, and R.P. Van Duyne, *J. Phys. Chem. B* **106** (2002) p. 853.
17. M. Litorja, C.L. Haynes, A.J. Haes, T.R. Jensen, and R.P. Van Duyne, *J. Phys. Chem. B* **105** (2001) p. 6907.
18. T.R. Jensen, M. Duval Malinsky, C.L. Haynes, and R.P. Van Duyne, *J. Phys. Chem. B* **104** (2000) p. 10549.
19. T.R. Jensen, R.P. Van Duyne, S.A. Johnson, and V.A. Maroni, *Appl. Spectrosc.* **54** (2000) p. 371.
20. A.M. Michaels, M. Nirmal, and L.E. Brus, *J. Am. Chem. Soc.* **121** (1999) p. 9932.
21. S. Schultz, D.R. Smith, J.J. Mock, and D.A. Schultz, *Proc. Natl. Acad. Sci. U.S.A.* **97** (2000) p. 996.
22. J. Yguerabide and E.E. Yguerabide, *Anal. Biochem.* **262** (1998) p. 157.
23. U. Kreibig and M. Vollmer, *Optical Properties of Metal Clusters, Vol. 25* (Springer-Verlag, Heidelberg, Germany, 1995).
24. C.L. Haynes and R.P. Van Duyne, *J. Phys. Chem. B* **105** (2001) p. 5599.
25. B.T. Draine and J.J. Goodman, *Astrophys. J.* **405** (1993) p. 685.
26. B.T. Draine and P.J. Flatau, *J. Opt. Soc. Am. A* **11** (1994) p. 1491.
27. W.-H. Yang, G.C. Schatz, and R.P. Van Duyne, *J. Chem. Phys.* **103** (1995) p. 869.
28. T.R. Jensen, M.L. Duval, L. Kelly, A. Lazarides, G.C. Schatz, and R.P. Van Duyne, *J. Phys. Chem. B* **103** (1999) p. 9846.
29. M. Duval Malinsky, L. Kelly, G.C. Schatz, and R.P. Van Duyne, *J. Am. Chem. Soc.* **123** (2001) p. 1471.
30. A.J. Haes, S. Zou, G.C. Schatz, and R.P. Van Duyne, *J. Phys. Chem. B* **108** (2004) p. 6961.
31. L.S. Jung, C.T. Campbell, T.M. Chinowsky, M.N. Mar, and S.S. Yee, *Langmuir* **14** (1998) p. 5636.
32. A.D. McFarland and R.P. Van Duyne, *Nano Lett.* **3** (2003) p. 1057.
33. A.J. Haes, S. Zou, G.C. Schatz, and R.P. Van Duyne, *J. Phys. Chem. B* **108** (2004) p. 109.
34. A.J. Haes and R.P Van Duyne, *J. Am. Chem. Soc.* **124** (2002) p. 10596.
35. J.C. Riboh, A.J. Haes, A.D. McFarland, C.R. Yonzon, and R.P. Van Duyne, *J. Phys. Chem. B* **107** (2003) p. 1772.
36. C.R. Yonzon, E. Jeoung, S. Zou, G.C. Schatz, M. Mrksich, and R.P. Van Duyne, *J. Am. Chem. Soc.* **126** (2004) p. 12669.
37. A.J. Haes, W.P. Hall, L. Chang, W.L. Klein, and R.P. Van Duyne, *Nano Lett.* **4** (2004) p. 1029.
38. A.J. Haes, L. Chang, W.L. Klein, and R.P. Van Duyne, *J. Am. Chem. Soc.* **127** (2005) p. 2264.
39. G. Raschke, S. Kowarik, T. Franzl, C. Soennichsen, T.A. Klar, J. Feldmann, A. Nichtl, and K. Kuerzinger, *Nano Lett.* **3** (2003) p. 935.
40. R.P. Van Duyne, A.J. Haes, and A.D. McFarland, *Proc. SPIE–The International Society for Optical Engineering* **5223** (2003) p. 197.
41. D.L. Jeanmaire and R.P. Van Duyne, *J. Electroanal. Chem.* **84** (1977) p. 1.
42. C.L. Haynes and R.P. Van Duyne, *J. Phys. Chem. B* **107** (2003) p. 7426.
43. S. Nie and S.R. Emory, *Science* **275** (1997) p. 1102.
44. K. Kneipp, Y. Wang, H. Kneipp, L.T. Perelman, I. Itzkan, R.R. Dasari, and M.S. Feld, *Phys. Rev. Lett.* **78** (1997) p. 1667.
45. P.F. Liao, J.G. Bergman, D.S. Chemla, A. Wokaun, J. Melngailis, A.M. Hawryluk, and N.P. Economou, *Chem. Phys. Lett.* **81** (1981) p. 355.
46. R.E. Howard, P.F. Liao, W.J. Skocpol, L.D. Jackel, and H.G. Craighead, *Science* **221** (1983) p. 117.
47. N. Felidj, S.L. Truong, J. Aubard, G. Levi, J.R. Krenn, A. Hohenau, A. Leitner, and F.R. Aussenegg, *J. Chem. Phys.* **120** (2004) p. 7141.
48. A.D. McFarland, "Using Nanoparticle Optics for Ultrasensitive Chemical Detection and Surface-Enhanced Spectroscopy," PhD thesis, Northwestern University, 2004.
49. A.D. McFarland, M.A. Young, J.A. Dieringer, and R.P. Van Duyne, *J. Phys. Chem. B* **109** (2005) accepted.
50. E. Hao and G.C. Schatz, *J. Chem. Phys.* **120** (2004) p. 357.
51. S. Zou, N. Janel, and G.C. Schatz, J. Chem. Phys. 120 (2004) p. 10871. □